Solid State Ionics 187 (2011) 8–18

Contents lists available at ScienceDirect

Solid State Ionics

journal homepage: www.elsevier.com/locate/ssi

Semi-ab initio interionic potential for gadolinia-doped ceria

Zhiwei Cui [a], Yi Sun [a,*], Yunjun Chen [a], Jianmin Qu [b]

[a] Department of Astronautic Science and Mechanics, Harbin Institute of Technology, Harbin, 150001, PR China
[b] Department of Mechanical Engineering, Northwestern University, Evanston, IL 60208, USA

ARTICLE INFO

Article history:
Received 3 March 2010
Received in revised form 24 November 2010
Accepted 8 February 2011
Available online 8 March 2011

Keywords:
Gadolinia-doped ceria
Lattice inversion
Quantum-chemical calculations
Molecular dynamics simulation

ABSTRACT

In the current work, a set of *semi-ab initio* interionic pair potentials in a concise functional form with parameters for gadolinia-doped ceria (GDC) systems is derived via the Chen–Mobius lattice inversion and *ab initio* quantum-chemical calculation. The quality of the proposed potentials is verified by molecular dynamics simulations of CeO_2 and A_2O_3 (A = Ce and Gd) on their static properties, doped concentrations and temperature dependence of lattice constants, mean-square displacements, pair correlation functions and elastic constants. Simulation results are consistent with corresponding experimental data, showing that the new form is valid over a wide range of interionic separations and applicable for describing structural properties of ionic solids.

1. Introduction

Solid electrolytes have received increasing attentions in recent years for their applications in solid oxide fuel cells (SOFC) or oxygen sensors. Among them, rare earth-doped ceria are widely used as the intermediate temperature electrolyte. The effects of doped ionic radius and concentrations to their electrical conductivity have been studied both by experiments and atomic scale simulations [1–3]. For example, Gd-doped ceria shows the maximum ionic conductivity due to the optimal ionic radius of Gd^{3+} (about 1.04 Å) [4]. However, under a low oxygen partial pressure, the matrix ceria experiences a volumetric expansion [5], resulting to a discharge of the uniformly charged Ce^{4+} to Ce^{3+}. During the discharging process, some additional oxygen vacancies are generated to keep electric neutrality. Obviously, such internal structural changes will diminish the mechanical performance of electrolyte [6].

To study the evolution behavior of non-stoichiometric GDC, the molecular dynamics (MD) method is adopted in this work. MD is proved to be a powerful technique to investigate the microscopic nature of atomic motion. With MD method, many literature works [7,8] have studied various properties of GDC. However, to the authors' best knowledge, all the potential functions adopted in the previous work, such as the Born–Mayer–Huggins form, were *a priori* [9–12]. And all their adjustable parameters are determined from the equilibrium and near-equilibrium properties. Note for non-stoichiometric GDC, different potential parameters may give divergent results. For example, with each own parameters, Inaba et al. [11] found that the GDC with Gd–Gd pairs was more stable than that with isolated Gd atoms; while Wei et al. [7] pointed out that the Gd^{3+} was distributed randomly in the ceria lattice. Similarly, Vyas's potential serves better for predicting the coefficient of compositional expansion (CCE); while Gotte's potential is more suitable for predicting the elastic constants [13]. Hence within the empirical potential framework, it is hard to determine a unique set of parameters yielding reasonable results for all the properties of interest. Some other form needs to be created.

Recently, Zhang and Chen [14,15] proposed a parameter-free method to determine the pairwise potential by lattice inversion. The potential form and all its parameters are directly evaluated from *ab initio* calculations. For instance, the effective charges on ions are determined at large lattice constant. With the aid of Chen–Mobius inversion, the short-range pairwise potential is derived from multiple lattice structures. Although the procedure is independent of experimental fitting data, some drawbacks still exist. Since the potentials between cations and anions have influence on the derivation of other potentials, some uncertainties exist and lead to different function form and parameters of the potential on the same species ions [15]. Therefore the lattice inversion method is limited to the solid solution with identical ions. On the other hand, the *ab initio* quantum-chemical calculation involved in the derivation of potential model of atom crystal [16,17] is performed with GAUSSIAN03 [18].

In this paper, we combine the lattice inversion and quantum-chemical calculation to derive the interionic pairwise potential of GDC. To simplify the derivation, the following assumptions are made about the system: (1) all ions are formally charged [9,10,12]; and (2) the cation–cation interactions are purely coulombic [9,10,12]. Note that the first assumption is to eliminate the influence of the difference charges on uniform ions caused by the charge determination. The idea is to first construct an extended phase space using cubic

* Corresponding author.
E-mail address: Sunyi@hit.edu.cn (Y. Sun).

0167-2738/$ – see front matter © 2011 Elsevier B.V. All rights reserved.
doi:10.1016/j.ssi.2011.02.008

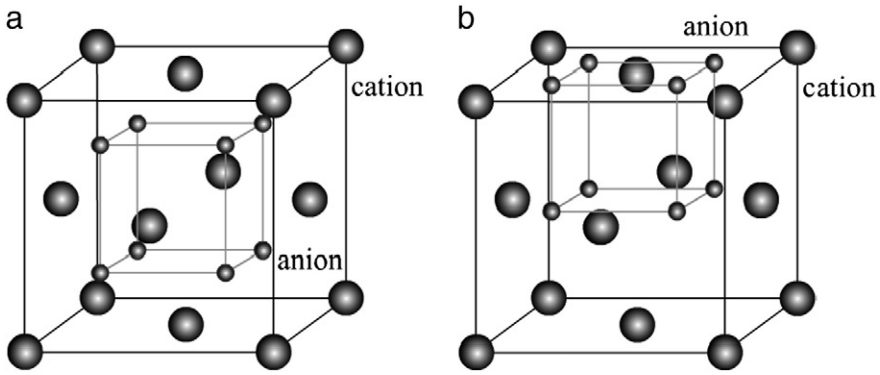

Fig. 1. Virtual structures used for the *ab initio* pseudopotential total-energy calculations of CeO_2. (a) T1 structure; and (b) T2 structure.

structures of CeO_2 and A_2O_3. Then the pseudopotential total-energy calculations are performed. After that, the short-range interactions between cations and anions are directly evaluated from a series of the total energy difference by lattice inversion. Finally, the function and parameters of the potential between O^{2-} ions can be fitted by quantum-chemical calculations.

The paper is organized as follows. In Section **2**, the interionic potential of GDC is derived. In Section **3**, several applications using the newly derived potential are given for verification purpose. Lattice constants, mean square displacements, pair correlation functions, coefficient of compositional expansion and elastic constants will be discussed in detail.

2. Derivation of interionic potential of GDC

Consider a system consisting of N ions. All ions are assumed to be formal charged for the sake of portability of the potential. The pairwise energy E^{pair} can be written as

$$E^{\text{pair}} = E^{\text{Coul}} + E^{\text{SP}}_{++} + E^{\text{SP}}_{--} + E^{\text{SP}}_{+-}, \tag{1}$$

where E^{Coul} is the Coulomb energy and E^{SP} is the short-range pairwise energy between ions. Coulomb energy can be evaluated by the Ewald summation technique or Wolf method [19]. However, terms on the right side of Eq. (1) cannot be calculated independently by only a single structure. Therefore virtual structures need to be introduced to cover more configurations and interionic spacings of our interest. These virtual structures must have identical sublattices constructed by cations and anions.

2.1. Virtual structural models

As stated above, virtual structural models are introduced in order to derive the proper interionic potentials between cations and anions from an extended phase space including equilibrium and non-equilibrium states. Here we concentrate on two types of virtual models for CeO_2 and A_2O_3 (A = Ce and Gd), respectively.

(1)CeO_2

At room temperature, pure ceria has the fluorite structure. Hence the prototypical structure of CeO_2 (T1 structure) is chosen to be fluorite structure. Another relevant structure (T2 structure) should be able to give the short-range interaction between Ce^{4+} and O^{2-}. These two structures have the same ion arrangement, i.e., the sublattice of cation is face-centered cubic (FCC) and that of anion is simple cubic (SC). T2 structure can be obtained by simply moving the sublattice of anion $0.25a$ along $\langle 100\rangle$, as shown in Fig. 1.

(2)$A_2O_3(A = Ce, Gd)$

Usually, Ce_2O_3 and Gd_2O_3 are of P-3M1 and IA-3, respectively. However, P-3M1 is a non-cubic structure, and the IA-3 is the cubic structure with 80 atoms. These two structures are not suitable for lattice inversion. Based on the description of interionic pair potentials, the interaction between two ions only depend on the interionic separation. Hence the interionic pair potentials are assumed as transferable in any structures. Here, the PN-3M structure is selected as the prototypical structure of A_2O_3 (T1 structure). The sublattice of cation is still FCC. Since the number of anions is only 6, less than that of ceria, the sublattice constructed by anion is IM-3M structure. The related structure (T2 structure) can be obtained by moving this sublattice of anion $0.25a$ along $\langle 100\rangle$, as shown in Fig. 2.

Since all these structures are complicated, the ratio of anions and cations is not 1:1, the coordination number of each ion should be calculated initially. Then the coefficients of inversion can be obtained, as described below.

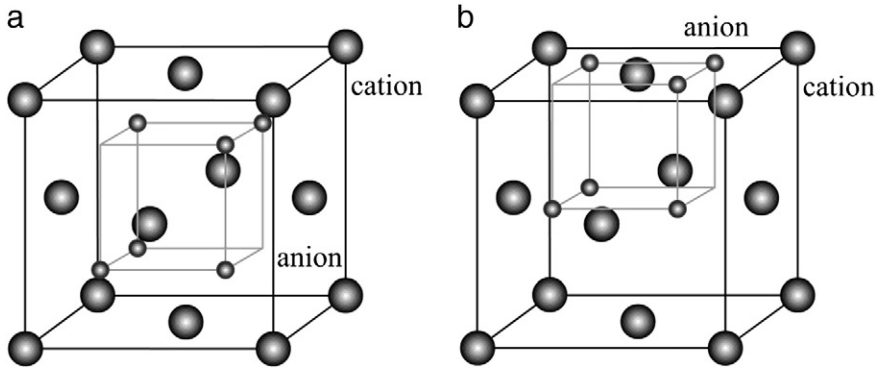

Fig. 2. Virtual structures used for the *ab initio* pseudopotential total-energy calculations of A_2O_3. (a) T1 structure; and (b) T2 structure.

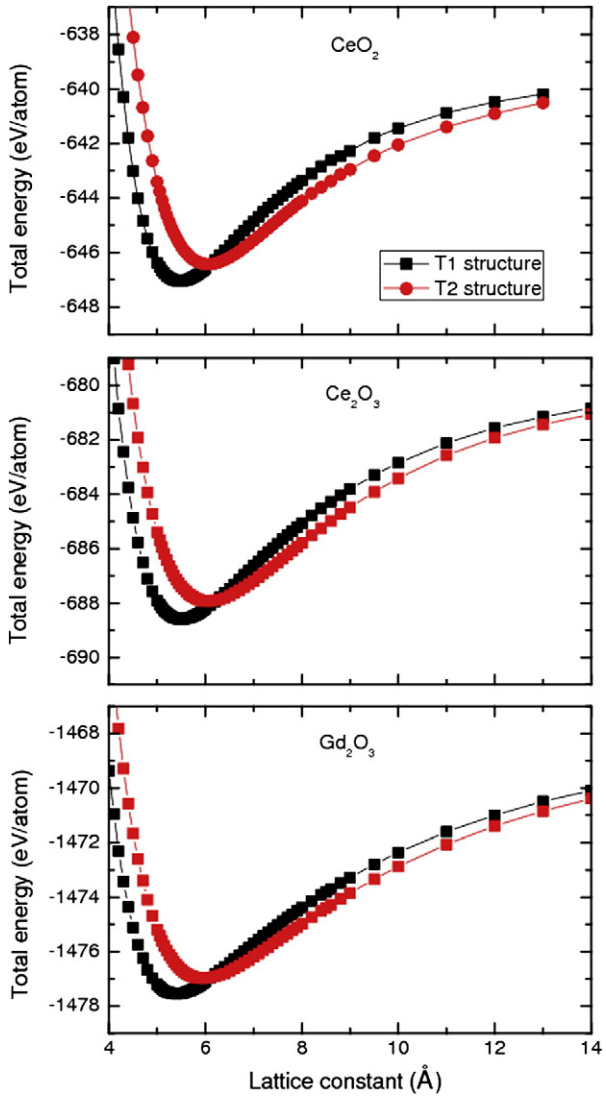

Fig. 3. CeO_2, Ce_2O_3 and Gd_2O_3 total energies versus lattice constant a in T1 and T2 structures from the *ab initio* calculations.

2.2. Lattice inversion for interionic potentials between cations and anions

Fig. 3 shows the total energies of those structures above versus lattice constant a, where $a = 4.0$–13.0 Å. They are calculated by ultrasoft pseudopotentials, together with Perdew–Burke–Ernzerhof (PBE) generalized gradient approximation (GGA) exchange, i.e., correlation function in the CASTEP program [20]. The k-mesh points over the Brillouin zone are generated with parameters $11\times11\times11$ for the biggest reciprocal space and $3\times3\times3$ for the smallest one by the Monkhorst–Pack scheme. A plane-wave basis set with 410 eV/atom cutoff is applied. The energy tolerance for self-consistent field (SCF) convergence is 5.0×10^{-7} eV/atom for all calculations.

The energy calculated by first principle and the potential employed in MD simulation can be connected by means of lattice inversion. Note in the above structures, the status of cations and anions are distinct due to the unbalanced ratio of anions and cations. For a crystal like A_xB_y, the relationship between energy from first principle and that obtained by MD simulation can be expressed as follows,

$$E^{\text{pair}}_{\text{CASTEP}} = \frac{1}{2}\frac{N_1E_{A-A} + N_2E_{B-B} + N_1E_{A-B} + N_2E_{B-A}}{N_1 + N_2}, \tag{2}$$

where N_1 and N_2 are the numbers of atoms A and B, respectively, and the four combinations $E_{\alpha-\beta}$ (α, β=A or B) denote the energy between site pairs of atom species (α, β). The leading factor 1/2 is due to double counting. For E_{A-B} and E_{B-A} are not necessarily the same, a relation of $N_1E_{A-B} = N_2E_{B-A}$ always holds. Denoting the coordination number of atom species α with neighbors of β as $(CN)_{\alpha-\beta}$, the relationship of the coordination number between species A and B is then

$$\frac{(CN)_{A-B}}{(CN)_{B-A}} = \frac{E_{A-B}}{E_{B-A}} = \frac{N_2}{N_1} = \frac{y}{x}. \tag{3}$$

For simplicity, atoms with small *CN* are regarded as the center ion in this paper. If $x>y$, Eq. (2) can be simplified to

$$E^{\text{pair}}_{\text{CASTEP}} = \frac{1}{2}\frac{N_1E_{A-A} + N_2E_{B-B} + 2N_1E_{A-B}}{N_1 + N_2}. \tag{4}$$

We then apply Eq. (4) to CeO_2 and A_2O_3.

(1)CeO_2

In CeO_2 fluorite structure, each Ce^{4+} cation is surrounded by eight O^{2-} ions forming the corners of a cube, while each O^{2-} has only four

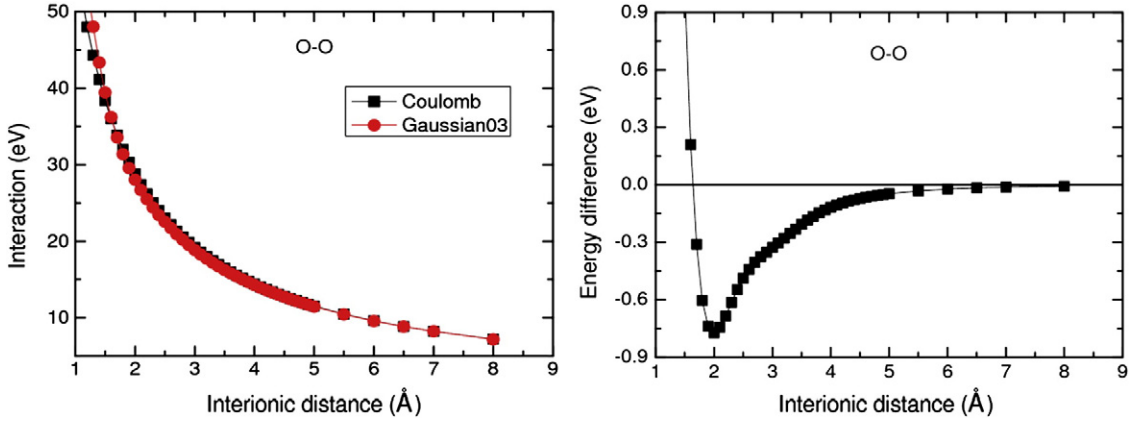

Fig. 4. O^{2-} energies versus interionic distance r_{ij} in the range of 1 to 8 Å compared with the *ab initio* calculations and Coulomb energy.

Table 1
The parameters of short-ranged potentials of CeO_2 and A_2O_3.

Species	a (eV)	b	c (Å)
O^{2-}–O^{2-}	0.77109	7.85216	1.99458
Ce^{4+}–O^{2-}	0.20	8.46211	3.42512
Ce^{3+}–O^{2-}	0.20	8.93524	3.25432
Gd^{3+}–O^{2-}	0.20	7.95857	3.40062

Ce^{4+} neighbors. Hence the ratio of cations and anions is 2:1. In ceria, the number of cation is assumed to be N, then Eq. (4) is

$$E^{\text{pair}}_{\text{CASTEP}} = \frac{1}{2}\frac{NE_{\text{Ce-Ce}} + 2NE_{\text{O-O}} + 4NE_{\text{O-Ce}}}{3N} = \frac{1}{2}\frac{E_{\text{Ce-Ce}} + 2E_{\text{O-O}} + 4E_{\text{O-Ce}}}{3}. \quad (5)$$

Since CeO_2 has two different structures T1 and T2, the short-range interaction energy should be determined for each of them based on Eq. (5). The results are as follows.

$$E^{\text{SP}}_{\text{T1}(+-)} = E^{\text{tot}}_{\text{T1}} - E^{\text{Coul}}_{\text{T1}} - E^{\text{iso}} = \frac{1}{2}\sum_{i,j,k}\frac{4}{3}\Phi^{\text{SP}}_{+-}\left[\sqrt{(i+j-0.5)^2 + (j+k-0.5)^2 + (k+i-0.5)^2}\,\frac{a}{2}\right] \quad (6)$$

$$E^{\text{SP}}_{\text{T2}(+-)} = E^{\text{tot}}_{\text{T2}} - E^{\text{Coul}}_{\text{T2}} - E^{\text{iso}} = \frac{1}{2}\sum_{i,j,k}\frac{4}{3}\Phi^{\text{SP}}_{+-}\left[\sqrt{(i+j-0.5)^2 + (j+k)^2 + (k+i-0.5)^2}\,\frac{a}{2}\right] \quad (7)$$

Note that here and after E^{tot} denotes the total energies obtained by CASTEP program, and E^{iso} denotes the energy of isolated ions, which is independent on the interionic separation.

(2)A_2O_3

Obviously, the ratio of cations and anions in A_2O_3 is 3:2. Taking the numbers of anion and cation as $3N$ and $2N$, respectively, the average energy per atom is then written as

$$E^{\text{pair}}_{\text{CASTEP}} = \frac{1}{2}\frac{2NE_{\text{A-A}} + 3NE_{\text{O-O}} + 6NE_{\text{O-A}}}{5N} = \frac{1}{2}\frac{2E_{\text{A-A}} + 3E_{\text{O-O}} + 6E_{\text{O-A}}}{5}. \quad (8)$$

Table 2
Static properties of CeO_2 under 0 K and 0 Pa.

	Lattice constant a_0 (Å)	Lattice energy E_{latt} (eV)	Bulk modulus B_0 (GPa)	Elastic constants (GPa)		
				C_{11}	C_{12}	C_{44}
This work	5.418	34.30	223.1	458.2	105.6	106.1
Gotte [12]	5.411	33.95	203.5	402	104	61
Vyas [10]	5.411	35.21	267.9	554.2	124.6	123.6
Butler [9]	5.411	35.22	263.6	504.4	143.1	16.1
CASTEP	5.465		174.8	330.2	97.1	46.4
Expt [21]	5.411		236.0	403	105	60

Table 3
Lattice constants of A_2O_3.

Lattice constant		This work	Gotte [12]	Vyas [10]	Minervini [34]	Expt
Ce_2O_3	a (Å)	3.902	3.889	3.858		3.891 [35]
	c (Å)	6.132	6.161	6.163		6.059 [35]
Gd_2O_3	a (Å)	10.790			10.805	10.810 [36]

With the same strategy, the short-range energy for T1 and T2 structures of A_2O_3 can be derived to be

$$E^{\text{SP}}_{\text{T1}(+-)} = E^{\text{tot}}_{\text{T1}} - E^{\text{Coul}}_{\text{T1}} - E^{\text{iso}} = \frac{1}{2}\sum_{i,j,k}\frac{6}{5}\Phi^{\text{SP}}_{+-}\left[\sqrt{(i+j-0.5)^2 + (j+k-0.5)^2 + (k+i-0.5)^2}\,\frac{a}{2}\right] \quad (9)$$

$$E^{\text{SP}}_{\text{T2}(+-)} = E^{\text{tot}}_{\text{T2}} - E^{\text{Coul}}_{\text{T2}} - E^{\text{iso}} = \frac{1}{2}\sum_{i,j,k}\frac{6}{5}\Phi^{\text{SP}}_{+-}\left[\sqrt{(i+j-0.5)^2 + (j+k)^2 + (k+i-0.5)^2}\,\frac{a}{2}\right] \quad (10)$$

In the above Eqs. (6)–(10), the short-range pairwise potential $\Phi^{\text{SP}}_{+-}(r_{ij})$ between cation and anion can be evaluated directly by Chen–Mobius lattice inversion. This is also true for evaluation of potentials between uniform ions. However, it is not practical for the case with atomic motion of solid solution due to their distinct forms and parameters. Hence the quantum-chemical method is adopted instead for potentials between same species ions.

2.3. Quantum-chemical calculation for potential between O^{2-} ions

In Ref. [17], Ohta et al. utilized quantum-chemical calculations to develop the potential model between atoms. They then use MD method to simulate the atomic-scale reaction dynamics of Si etching processes by Br^+-containing plasmas. Even their work involves only charge-neutral species, their technique motivates the current work on the potential between O^{2-} ions.

To carry out the calculation, we first impose the adiabatic assumption for electron dynamics (Born–Oppenheimer approximation). Then the interionic forces can be obtained from the derivatives of potential functions with respect to the position of the nucleus. For quantum-chemical calculations, we use the general purpose software GAUSSIAN03 [18]. A correlation method QCISD(T, Full)/6-311G(2df) is adopted as the model chemistry and basis set. In order to obtain the short-range interaction between O^{2-} ions, the total charge and the spin multiplicity

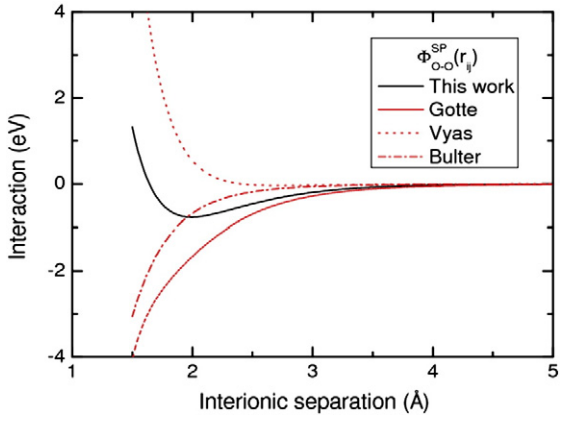

Fig. 5. The comparison of different interactions of O^{2-}–O^{2-}.

S (number of lone pair electrons + 1) for each ion configuration should be specified. Determination of the potential involves the following two steps: (1) determination of the isolated O^{2-} energy; and (2) comparison with pair O^{2-} ions energy and formal charged (−2) Coulomb energy. Fig. 4 shows these energies corresponding to the interionic separation r_{ij}. The difference between Coulomb and *ab initio* calculations is assumed to be not significant if r_{ij}>5 Å, i.e., the interaction between two uniform ions is purely coulombic for interionic distance greater than 5 Å.

Based on the above strategies, the short-range interionic pair potential can be evaluated from lattice inversion and quantum-chemical technique. Fitting processes to the obtained potential curves then give suitable potential function forms accordingly, as stated below:

$$\Phi_{+-}(r) = \Phi^{SP}_{+-}(r) + \Phi^{Coul}_{+-}(r) \tag{11}$$
$$= a_{+-}\exp\left[b_{+-}\left(1-\frac{r}{c_{+-}}\right)\right] + \frac{q_+q_-}{4\pi\varepsilon_0 r}$$

$$\Phi_{--}(r) = \Phi^{SP}_{--}(r) + \Phi^{Coul}_{--}(r) \tag{12}$$
$$= a_{--}\left\{\left(\exp\left[\frac{b_{--}}{2}\left(1-\frac{r}{c_{--}}\right)\right]-1\right)^2-1\right\} + \frac{q_-^2}{4\pi\varepsilon_0 r}$$

$$\Phi_{++}(r) = \Phi^{Coul}_{++}(r) = \frac{q_+^2}{4\pi\varepsilon_0 r} \tag{13}$$

where, $\Phi^{SP}_{+-}(r)$ is the exponent repulsive part and $\Phi^{SP}_{--}(r)$ is the Morse function. The involved parameters *a*, *b*, and *c* for different cases are tabulated in Table 1.

3. Application of interionic potentials

In this section, the above developed interionic potentials are applied to carry out several verifications. Each test is given in a subsection.

3.1. Static properties of CeO_2 and A_2O_3 at 0 K under no pressure

We first calculate the static properties of equilibrium CeO_2 and A_2O_3 at zero temperature and pressure. Lattice constants, lattice energy, and elastic properties have also been calculated based on the CASTEP calculation and other empirical functions. The results are given in Tables 2 and 3.

All results, including the current one and those from empirical potentials by Gotte [12], Vyas [10] and Butler [9] fit the experiment data [21] reasonably well. All the latter three potentials utilize the same potential function form, but with different parameters. It is well known that empirical potential depends strongly on the chosen set of fitting properties, hence may not reproduce other properties not in the set nicely. For instance, Butler's potential is fitted from many crystals. Lack of experiment data at that time, the lattice constant of GDC is much larger than experiment data. Similarly, Vyas's potential overestimates the mechanical constants since it is fitted from surface properties. In addition, Vyas's potential has parameters for Ce^{3+}–O^{2-} identical to that for Ce^{4+}–O^{2-}, thus failing to describe the structure of Ce_2O_3 accurately. Recently, Gotte employs most properties of CeO_2 and Ce_2O_3 to fit the potential parameters. However, his potential gives larger conductivity and lower CCE values [13] than the experimental ones. In short, empirical potential may not describe the structure evolution properly in extended phase space.

We also compare the short-range potential curves of O^{2-}–O^{2-} using all the potentials mentioned above, as shown in Fig. 5. At the nearest distance of O^{2-}–O^{2-} in CeO_2, i.e., 2.7 Å, all the potentials are in attractive sense. However, the interactions of O^{2-}–O^{2-} in Butler's and Vyas' potential are very weak, leading to minor effect of the short-range potentials to material properties. This case is improved in Gotte's potential, where a stronger O^{2-}–O^{2-} interaction leads to better mechanical constants. Unlike the adjustable parameters in empirical potentials, our potential features are fixed magnitude of interaction. This is due to the *ab initio* nature while selecting the forms and parameters.

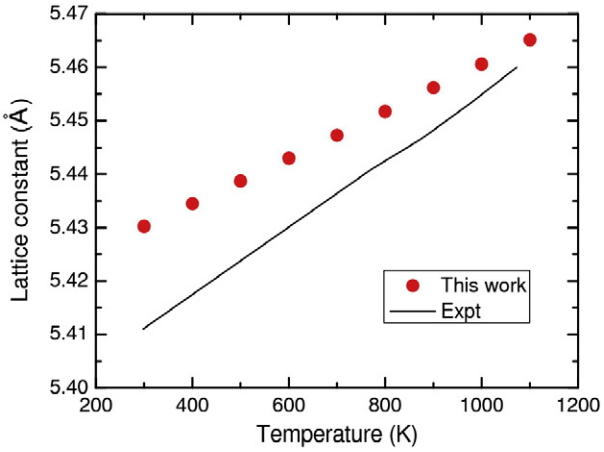

Fig. 7. The temperature dependence of the lattice constant from 300 to 1200 K. Temperature step is 100 K.

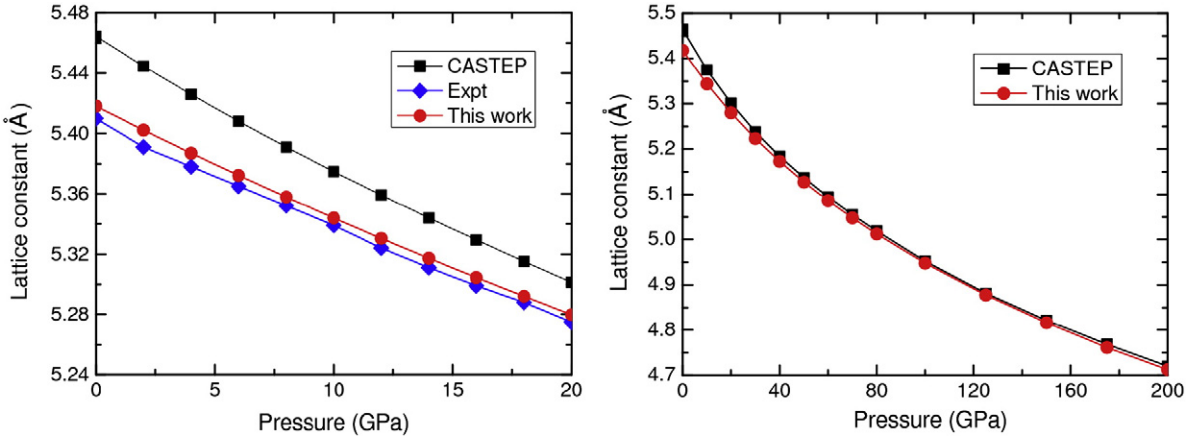

Fig. 6. The pressure dependence of the lattice constant from 0 to 200 GPa.

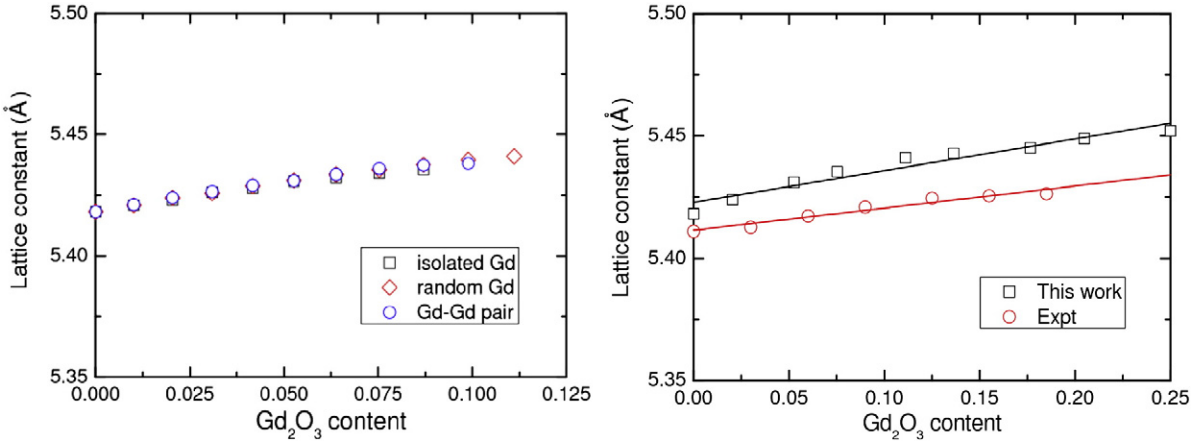

Fig. 8. Calculated and observed lattice parameters of GDC as a function of Gd_2O_3 content.

3.2. CeO_2 at 0 K under high pressure

To better assess the developed *ab initio* potential, we now extend the system pressure from zero to a finite wide range and calculate the lattice parameters of CeO_2. The results are depicted in Fig. 6. In the pressure range from 0 to 20 GPa, our results are in good agreement with experiment data [22]. For a even larger range of 20–200 GPa, where experimental data are absent, our calculation and CASTEP share the same trend, with the CASTEP one slightly larger than ours. This is due to a larger lattice constant by CASTEP calculation at zero temperature and pressure than that from experiments. Also, note that from 0 to 200 GPa, the lattice constant reduces gradually from 5.4 Å to 4.7 Å. This reveals that our interionic potential could describe the evolution of material behaviors in extended phase space.

3.3. CeO_2 at high temperatures

We now raise the system temperature to a finite one. For finite temperature, the molecular mechanics method is not appropriate so MD simulations are adopted instead. The simulation system includes 1500 ions ($5\times5\times5$ CeO_2 supercell). The NPT ensemble is adopted, implemented by Nose–Poincare thermostat [23], metric-tensor pressostat [24], and generalized leap-frog algorithm [25] for the time integration. Wolf algorithm [19] is used to estimate the Coulomb interaction. The cutoff distance is set as 10.82 Å. Each simulation is equilibrated for 1×10^6 steps. And additional 2×10^6 steps are evolved for data collection.

With the above MD setup, lattice constants are calculated in the temperature range of 300–1200 K, as shown in Fig. 7. Both calculation and experiment give the same trend. The smaller slope of the calculation result indicates that the coefficient of thermal expansion by calculation is smaller than the corresponding experiment data [26]. This is mainly due to the formal-charge assumption. A potential proposed by Inaba et al. [11] accounts for the fractional charge (0.675 of the formal charge) and considers the lattice constants of both normal and high temperatures in the fitting procedure. It is believed that such a potential with a small fractional charge attenuating the attraction between anions and cations may reproduce a better thermal expansion coefficient.

3.4. GDC structure

GDC consists of the basis CeO_2 and the dopant Gd_2O_3. Such a doping process can be represented as follows

$$Gd_2O_3 \xrightarrow{CeO_2} 2Gd'_{Ce} + V_O^{\bullet\bullet} + 3O_O^X. \quad (14)$$

The dopant Gd is trivalent ion. When two Gd ions replace the positions of two Ce ions, one oxygen vacancy is generated to keep the charge neutrality. In MD simulations, the GDC structure is constructed via three steps: (1) build the CeO_2 structure with $5\times5\times5$ supercells; (2) replace some Ce^{4+} ions by Gd^{3+} ions; and (3) remove some O^{2-} ions to form vacancies. To keep the electric neutrality, the compound always has the chemical formula of $(CeO_2)_{1-x}(Gd_2O_3)_{x/2}$ with various doping ratios. Due to the randomization of the doping procedure, we give three patterns to decide the arrangement mode of Gd^{3+} ions: 1) isolated Gd^{3+} ions, 2) random distribution, and 3) isolated Gd^{3+}–Gd^{3+} ion-pair. With the three ways, the relationships between lattice constants and Gd_2O_3 concentration for all these three patterns are depicted in Fig. 8. When

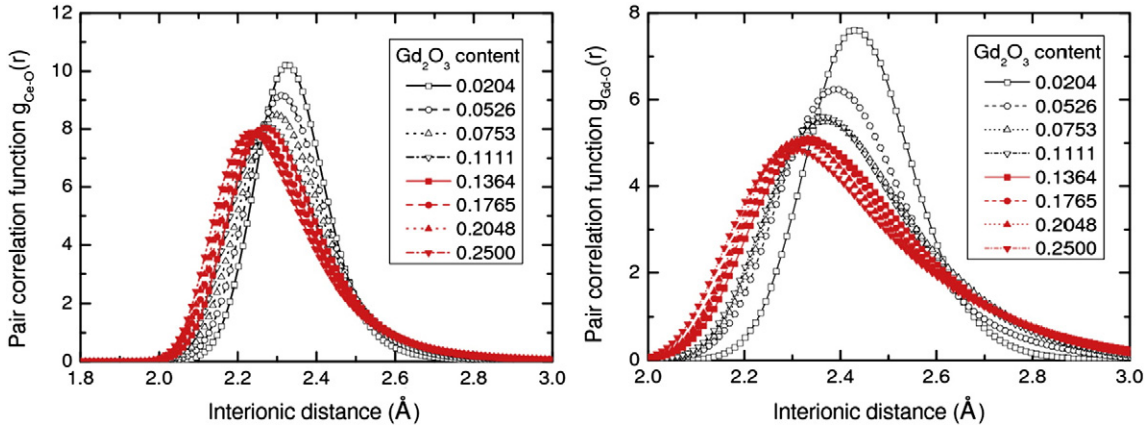

Fig. 9. Pair correlation functions of Ce–O and Gd–O as a function of Gd_2O_3 content.

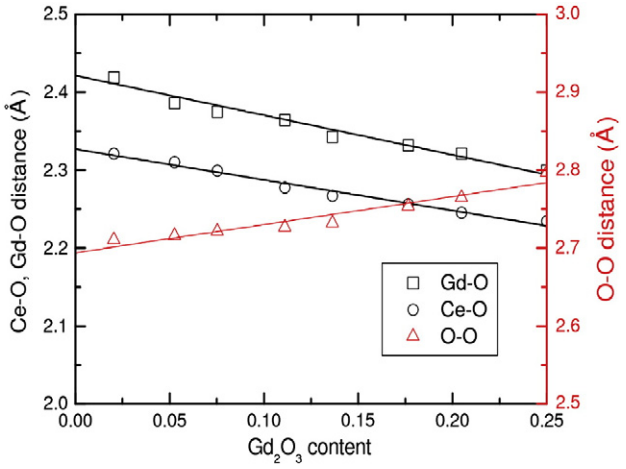

Fig. 10. Nearest distances of Ce–O, Gd–O, O–O as a function of Gd_2O_3 content.

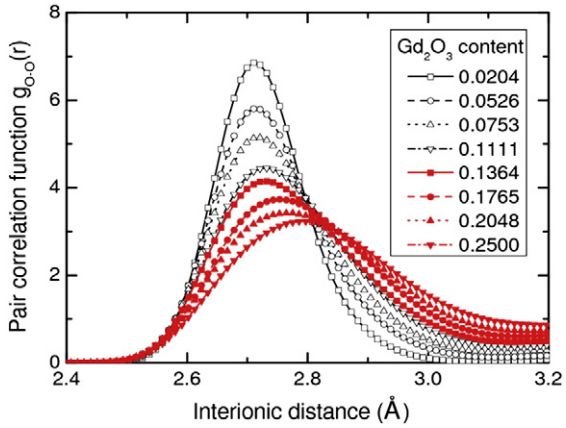

Fig. 11. Pair correlation functions of O–O as a function of Gd_2O_3 content.

doping concentration is greater than 0.1, pattern (1) and pattern (3) cannot exist due to an excess of dopant ions. In fact, the max doping concentration of pattern (1) is about 14.3 mol%, corresponding to the chemical formula $Ce_{0.75}Gd_{0.25}O_{1.875}$. Under certain circumstances, the distribution of Gd^{3+} is sole. Thus the 10 mol% of doping content is close to the limitation under random distribution situation.

When the doping concentration is less than 0.1, the difference of lattice constants between the three patterns can be neglected. This consequence perfectly matches the EXAFS data [27] and other simulation results [7]. In the following GDC calculations, pattern (2) is adopted to determine the Gd^{3+} ion distribution. The simulation results fit well with the experiment data [28] in the doping concentration range of 0–0.25 (Fig. 8).

3.5. Pair correlation functions in GDC

In order to investigate the microscopic structure, the pair correlation functions (PCF) of all pairs of ions are calculated by

$$g\left(r_{ij}\right) = \frac{n_{ij}(r)}{4\pi\left(N_i N_j / V\right) r^2 \Delta r} \tag{15}$$

where, N_i and N_j are the numbers of ion i and j, respectively. V is the volume of the system. $n_{ij}(r)$ is the number of the pair of ion i and ion j between the distance of $(r-\Delta r/2)$ and $(r+\Delta r/2)$.

We concentrate on the first peaks of Ce–O and Gd–O as a function of the doping concentration at 300 K. The results are shown in Fig. 9. The nearest cation–anion distances decrease with the increasing gadolinia content. And Ce–O distance is smaller than Gd–O distance at all gadolinia contents (Fig. 10). This might be due to the stronger Coulomb interaction of Ce–O than that of Gd–O. Simulation results match perfectly with the EXAFS data [29]. From Table 4, the distances between cations decrease gradually with increasing gadolinia contents. Furthermore, the PCFs of O–O for various gadolinia contents are shown in Fig. 11. The greater nearest distance of O–O and the broadening of the peaks are observed with increasing doping content. Such broadening indicates that various kinds of oxygen sites become possible. When the nearest distance is greater than 3 Å, the PCF of high doping concentration is far from 0, implying that the site of oxygen ion deviates from its original position.

Table 4
Nearest-neighbor distance between cations as a function of Gd_2O_3 content.

Content of Gd_2O_3	Nearest neighbor distance (Å)		
	Ce–Ce	Ce–Gd	Gd–Gd
0.0204	3.8357	3.8248	3.7815
0.0526	3.8357	3.8248	3.7707
0.0753	3.8357	3.8248	3.8032
0.1111	3.8357	3.8140	3.7707
0.1364	3.8249	3.8120	3.7924
0.1755	3.8229	3.8033	3.7815
0.2048	3.8140	3.8002	3.7707
0.2500	3.8032	3.7924	3.7599

The *CN* can be obtained by integrating the PCF, as shown in Fig. 12. The *CN*s of Gd^{3+} and Ce^{4+} are analogical, i.e., the vacancy opts not to be adjacent to any cations. This result is different from the conclusion of Inaba et al. In Ref. [11], the Gd–Gd pair is the optimal arrangement mode. And the Gd^{3+}-vacancy-Gd^{3+} cluster is most likely the practical defect for GDC. However, the current work shows that the random distribution of Gd^{3+} ions is more reasonable. The association energy between Gd–Gd is not measurable, thus the Gd^{3+}-vacancy-Gd^{3+} cluster with $CN=7$ doesn't exist with the current potential. The *CN* being between 7 and 8 of Ce^{4+} and Gd^{3+} indicates that the cation-vacancy cluster may not be stabilized. This agrees with Wei's conclusions [7].

3.6. Mean square displacement in GDC

The mean square displacement can be evaluated by

$$\mathrm{msd}(t) = \frac{\sum\left\langle\left[\vec{r}_i(t)-\vec{r}_i(0)\right]^2\right\rangle}{N} \tag{16}$$

where, N is the number of ions, $\vec{r}_i$ is the position vector of ion i. Notation $\langle\rangle$ stands for averaging over all times. It is obvious that msd

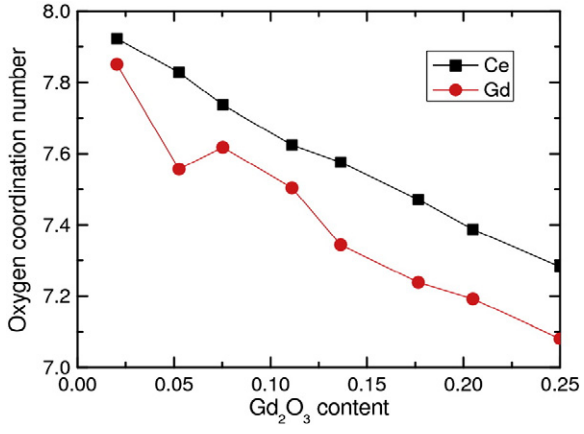

Fig. 12. Coordinate number of Ce^{4+} and Gd^{3+} as a function of Gd_2O_3 content.

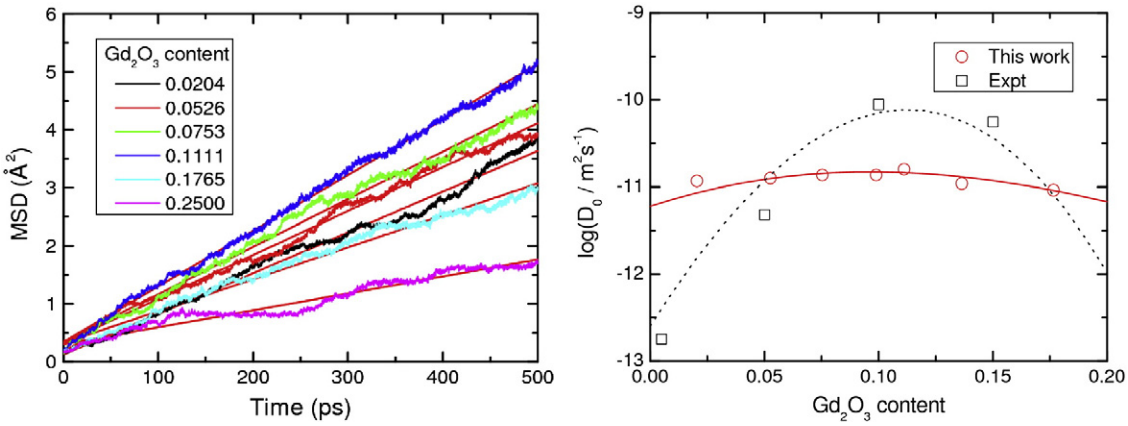

Fig. 13. Mean square displacement and diffusion coefficient of O^{2-} as a function of Gd_2O_3 content.

(t) is proportional to the time t. By Einstein diffusion equation, one gets

$$\lim_{t\to\infty}[\mathrm{msd}(t)] = B + 6D\Delta t \tag{17}$$

where D is the diffusion coefficient. The slope of msd curve is $6D$. Here we calculate the msd curve as a function of doping content at 1000 K, as depicted in Fig. 13. The msd curve initially increases, followed by a descending segment with increasing gadolinia content. The maximum of msd is acquired at a doping concentration of 11.11 mol%. The chemical formula is found to be $Ce_{0.8}Gd_{0.2}O_{1.9}$, matching well with experimental values [30].

By definition, diffusion coefficient D can be evaluated straightforwardly by taking the slope of the msd curve. The experiment data [30] can be used to find the diffusion constant by the Nernst–Einstein relation. Since the ionic conductivity is proportional to D, a large D means a large conductivity.

It is obvious that there exists a maximum ionic conductivity. We argue that it is the trade-off effect between the increasing vacancy sites and decreasing vacancy mobility with increasing Gd_2O_3 concentration. To see this, we divide the diffusion constant by the number of vacancy. This gives conductivity per single vacancy, as shown in Fig. 14. It is clear that the averaged conductivity decreases continuously with increasing Gd_2O_3 content. The temperature dependence of diffusion constant is of great interest. To accomplish this, we take 20GDC ($Ce_{0.8}Gd_{0.2}O_{1.9}$, which has the maximum diffusion constant) to calculate msd for a temperature range of 800–2000 K. Results are depicted in Fig. 15, showing that the slope of msd increases with a higher temperature, i.e., the ionic conductivity follows the sense of change of temperature. Assuming that the Arrhenius relation Eq. (18) holds, the activation energy (E_a) and the temperature independent prefactor (D_0) can be obtained. As a comparison, other MD simulation results of YDC (Yttria-doped ceria), LDC (Lanthanun-doped ceria) and reduced CeO_2 are listed in Table 5.

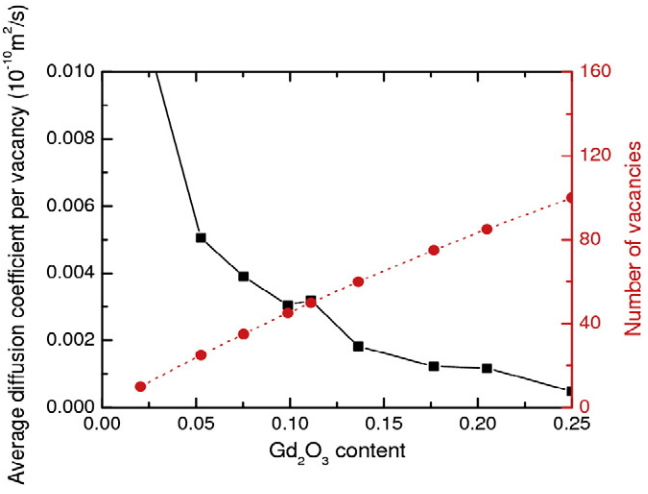

Fig. 14. Ionic conductivity per single vacancy.

$$D(T) = D_0 \exp\left(\frac{-E_a}{RT}\right) \tag{18}$$

3.7. CCE of Non-stoichiometric GDC

In this section, we discuss the CCE of non-stoichiometric GDC. The non-stoichiometric GDC is produced by putting extra vacancies besides the original ones introduced by dopant. The additional vacancy concentration can be created in stoichiometric GDC when it is exposed to a low partial pressure of oxygen. Such reduction is represented as

$$O_O^X \leftrightarrow V_O^{\bullet\bullet} + 2e' + \frac{1}{2}O_2. \tag{19}$$

The defect reaction generates Ce^{3+} instead of Ce^{4+} and proportional oxygen vacancies. This indicates that the total number of ions decreases. The effect of this chemical change on the mechanical property can be quantified by CCE and elastic constants, given that the deviation from stoichiometry is not too significant.

Here, we calculate the properties of 10GDC ($Ce_{0.9}Gd_{0.1}O_{1.95}$) and 20GDC ($Ce_{0.8}Gd_{0.2}O_{1.9}$), where gadolinium atoms replace 10% and 20% of the cerium sites in ceria, respectively. Their corresponding non-stoichiometric forms are $Ce_{0.9}Gd_{0.1}O_{1.95-\delta}$ and $Ce_{0.8}Gd_{0.2}O_{1.9-\delta}$, where the subscript δ marks the additional oxygen vacancy concentration.

When δ is small, CCE, denoted by η, is defined as the linear strain per deviation from stoichiometry, i.e.

$$\eta = \left.\frac{\partial \varepsilon_L}{\partial \rho}\right|_{\rho=\rho_0} \tag{20}$$

where, ε_L is the linear chemical expansion and ρ is the vacancy concentration. $\delta = \rho - \rho_0$ is the deviation from stoichiometry. Since the non-stoichiometric GDC can be considered as the dopant Ce_2O_3 into GDC, we still employ the method that constructs the GDC structure to produce the non-stoichiometric GDC structure. After the structure optimization, the shape of system remains cubic, i.e., the

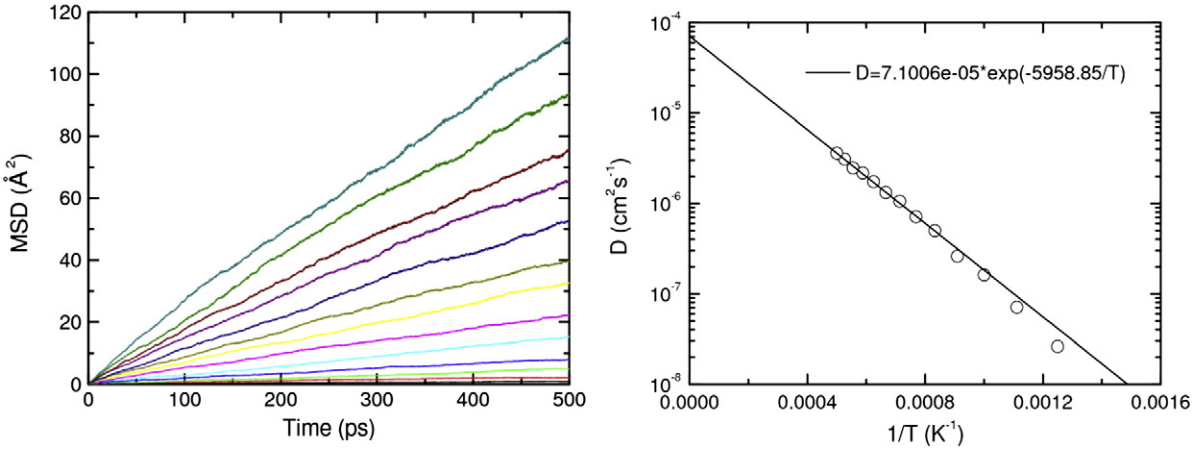

Fig. 15. Mean square displacement of 20GDC as a function of temperature.

strain induced as a result of non-stoichiometry is purely volumetric. Thus the linear strain can be evaluated as

$$\varepsilon_L = \frac{V(\delta)-V(0)}{3V(0)}. \tag{21}$$

Fig. 16 depicts the relation ε_L versus δ. The results fit well with experiment data [6]. Moreover, ε_L is proportional to the δ, leading to $\eta = \varepsilon_L/\delta$ by Eq. (18). The values of CCE for 10GDC and 20GDC are given in Table 6.

3.8. Elastic constants of non-stoichiometric GDC

Non-stoichiometric GDC has a cubic structure, hence it has three independent elastic constants C_{11}, C_{12} and C_{44}. These constants can be calculated directly with the stress-strain fluctuation formula [31]. Results for 10GDC and 20GDC are shown in Fig. 17. Note for both GDCs, C_{11} decreases rapidly with increasing δ. This is due to the weaker Coulomb interaction with larger deviation from stoichiometry. Note also that the elastic constants of 10GDC are larger than the correspondent ones of 20GDC. It is the consequence of lower oxygen vacancy concentration in the former. The δ dependence of C_{12} and C_{44} is small and can be safely neglected.

Besides the properties of single crystals, the elastic constants of isotropic polycrystalline GDC should be calculated for its applications in SOFC. The polycrystalline properties are obtained by using a homogenization method [32]. The bulk modulus of such an aggregate is well defined, whereas the shear modulus is inherently uncertain, depending on details of the arrangement and shape of the constituent crystals. The bulk modulus is related to the elastic constants by

$$K = \frac{C_{11} + 2C_{12}}{3}. \tag{22}$$

Table 5
Oxygen diffusion data from the present study compared with values for various results from experiments and from MD simulations.

Sample	D_0 (cm²/s)	D (cm²/s)	E_a (kJ/mol)	T (K)	Ref.
$Ce_{0.8}Gd_{0.2}O_{1.9}$	$7.1\cdot10^{-5}$		49.5	800–2000	This work
$Ce_{0.8}Gd_{0.2}O_{1.9}$		$6.6\cdot10^{-7}$		1273	This work
$Ce_{0.8}Y_{0.2}O_{1.9}$		$3.6\cdot10^{-7}$		1273	Ref. [37]
$Ce_{0.8}Y_{0.2}O_{1.9}$		$1.1\cdot10^{-7}$		1273	Ref. [38]
$Ce_{0.76}La_{0.24}O_{1.88}$		$1.3\cdot10^{-7}$		1273	Ref. [38]
$Ce_{0.8}Gd_{0.2}O_{1.9}$		$2.4\cdot10^{-7}$		1273	Ref. [38]
$Ce_{0.8}Gd_{0.2}O_{1.9}$		$2.5\cdot10^{-7}$	44.0	1073	Ref. [1]
$Ce_{0.8}Gd_{0.2}O_{1.9}$		$8.9\cdot10^{-7}$		1273	Ref. [30]
$CeO_{1.8778}$	$5.7\cdot10^{-5}$		55.7	800–2200	Ref. [12]
$CeO_{1.8778}$		$2.6\cdot10^{-7}$		1250	Ref. [12]

The isotropic shear modulus in the Hashin–Shtrikman averaging scheme is given by

$$G = \frac{G_U + G_L}{2} \tag{23}$$

where the upper and lower bounds are

$$G_U = C_{44} + 2\left(\frac{5}{C_S - C_{44}} + \frac{18(K + 2C_{44})}{5C_{44}(3K + 4C_{44})}\right) \tag{24}$$

$$G_L = C_S + 3\left(\frac{5}{C_{44} - C_S} + \frac{12(K + 2C_S)}{5C_S(3K + 4C_S)}\right) \tag{25}$$

where $C_S = (C_{11} - C_{12})/2$. The elastic constants of polycrystalline can be represented more conveniently by two familiar engineering properties, Young's modulus and Poisson's ratio. Calculation results and experiment data [33] have been presented in Fig. 18. Young's modulus decreases with increasing deviation of stoichiometry.

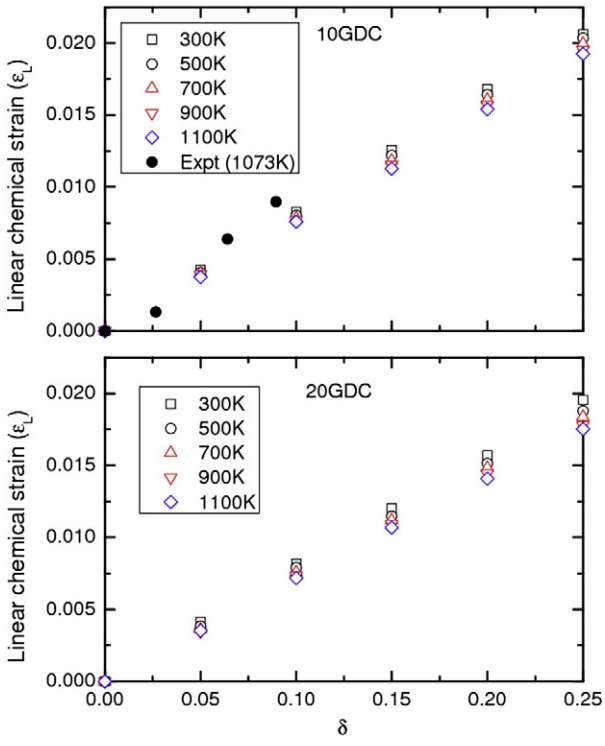

Fig. 16. Compositional strain versus δ of 10GDC and 20GDC.

Table 6
Average CCE values of 10GDC and 20GDC at various temperatures.

Temperature (K)	CCE	
	10GDC	20GDC
300	0.08279	0.07792
500	0.08179	0.07511
700	0.07994	0.07376
900	0.07826	0.07167
1100	0.07709	0.07012

However, Young's modulus and its variation with stoichiometry do not show strong temperature dependence. Further, it is found that Poisson's ratio is about 0.26 and varies within 6% over the whole range of temperature and non-stoichiometry considered here.

4. Concluding remarks

In this paper, we propose a novel method to derive the interionic potentials of CeO_2, Gd_2O_3 and Ce_2O_3 based on the *ab initio* calculations. Pairs of hetero- and homo-species ions are handled by multiple lattice inversion and quantum chemistry. The newly developed potentials are verified by a bunch of MD simulations in various categories on CeO_2, GDC and non-stoichiometric GDC against experimental data. Simulation results prove that the proposed potential is reasonably good to be used for broad atomic simulations of materials with involved ions.

There are several issues that have not been resolved in the current work yet. First, the pairwise interaction is employed in this paper, which will lead to the unphysical Cauchy relation, i.e., $C_{12}=C_{44}$. Second, only limited applications of this algorithm are demonstrated. More cases need to be explored, such as Al_2O_3 or PbO_2. All these will be addressed in a future work.

In closing since all the ions are assumed to be formally charged, it will cause some inaccuracy in some properties, such as the thermal expansion coefficient of CeO_2. If a better charge determination is developed, we may have the confidence of better results. Therefore, these new interionic potentials may be promising in exploring and predicting the properties of ionic crystals and this new method is worth further refinement and extending to other ionic crystals.

Acknowledgments

This work was supported by National Natural Science Foundation of China (10972066) and the Foundation of Excellent Youth of

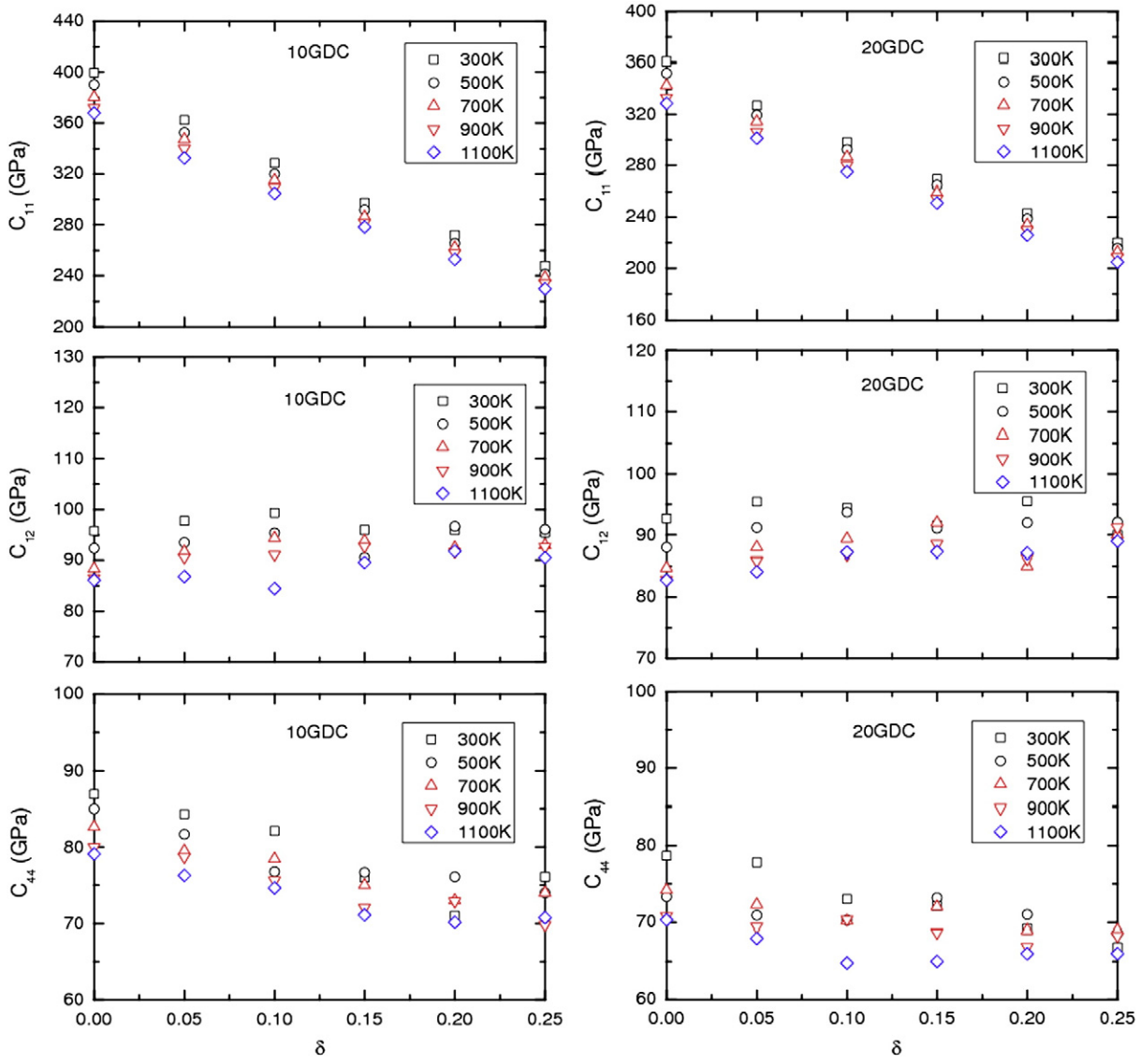

Fig. 17. Elastic constants versus δ of 10GDC and 20GDC.

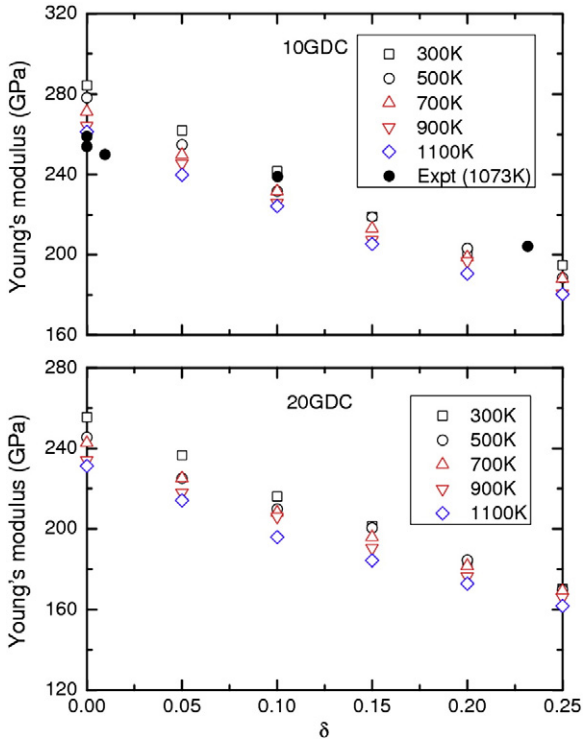

Fig. 18. Young modulus versus δ of 10GDC and 20GDC.

Heilongjiang Province. The authors would like to thank Dr. Yubao Zhen for helpful discussions.

References

[1] H. Yahiro, K. Eguchi, H. Arai, Solid State Ionics 36 (1989) 71.
[2] K. Eguchi, T. Setoguchi, T. Inoue, H. Arai, Solid State Ionics 52 (1992) 165.
[3] H. Inaba, H. Tagawa, Solid State Ionics 83 (1996) 1.
[4] D.-J. Kim, J. Am. Ceram. Soc. 72 (1989) 1415.
[5] A. Atkinson, Solid State Ionics 95 (1997) 249.
[6] K.L. Duncan, Y.L. Wang, S.R. Bishop, F. Ebrahimi, E.D. Wachsman, J. Am. Ceram. Soc. 89 (2006) 3162.
[7] X. Wei, W. Pan, L.F. Cheng, B. Li, Solid State Ionics 180 (2009) 13.
[8] M. Mogensen, N.M. Sammes, G.A. Tompsett, Solid State Ionics 129 (2000) 63.
[9] V. Butler, C. Catlow, B. Fender, J. Harding, Solid State Ionics 8 (1983) 109.
[10] S. Vyas, R.W. Grimes, D.H. Gay, A.L. Rohl, J. Chem. Soc. Faraday Trans. 94 (1998) 427.
[11] H. Inaba, R. Sagawa, H. Hayashi, K. Kawamura, Solid State Ionics 122 (1999) 95.
[12] A. Gotte, D. Spangberg, K. Hermansson, M. Baudin, Solid State Ionics 178 (2007) 1421.
[13] N. Swaminathan, J. Qu, Model. Simul. Mater. Sci. Eng. 17 (2009) 045006.
[14] S. Zhang, N.X. Chen, Phys. Rev. B 66 (2002) 064106.
[15] S. Zhang, N.X. Chen, J. Chem. Phys. 118 (2003) 3974.
[16] H. Ohta, S. Hamaguchi, J. Chem. Phys. 115 (2001) 6679.
[17] H. Ohta, A. Iwakawa, K. Eriguchi, K. Ono, J. Appl. Phys. 104 (2008) 073302.
[18] M.J. Frisch, G.W. Trucks, H.B. Schlegel, et al., Gaussian, Inc., Pittsburgh PA, 2003.
[19] D. Wolf, P. Keblinski, S.R. Phillpot, J. Eggebrecht, J. Chem. Phys. 110 (1999) 8254.
[20] S.J. Clark, M.D. Segall, C.J. Pickard, P.J. Hasnip, M.J. Probert, K. Refson, M.C. Payne, Z. Kristallogr. 220 (2005) 567.
[21] A. Nakajima, A. Yoshihara, M. Ishigame, Phys. Rev. B 50 (1994) 13297.
[22] L. Gerward, J.S. Olsen, L. Petit, G. Vaitheeswaran, V. Kanchana, A. Svane, J. Alloy. Compd. 400 (2005) 56.
[23] S.D. Bond, B.J. Leimkuhler, B.B. Laird, J. Comput. Phys. 151 (1999) 114.
[24] I. Souza, J.L. Martins, Phys. Rev. B 55 (1997) 8733.
[25] G. Sun, J. Comput. Math. 3 (1993) 250.
[26] M. Dudek, J. Eur. Ceram. Soc. 28 (2008) 965.
[27] H. Deguchi, H. Yoshida, T. Inagaki, M. Horiuchi, Solid State Ionics 176 (2005) 1817.
[28] D. Bevan, E. Summerville, Handbook on the Physics and Chemistry on Rare Earth's, vol. 4, North-Holland, Amsterdam, 1979.
[29] T. Ohashi, S. Yamazaki, T. Tokunaga, Y. Arita, T. Matsui, T. Harami, K. Kobayashi, Solid State Ionics 113–115 (1998) 559.
[30] J. Faber, C. Geoffroy, A. Roux, A. Sylvestre, P. Abelard, Appl. Phys. A 49 (1989) 225.
[31] Z. Cui, Y. Sun, J. Li, J. Qu, Phys. Rev. B 75 (2007) 214101.
[32] B.B. Karki, L. Stixrude, S.J. Clark, M.C. Warren, G.J. Ackland, J. Crain, Am. Mineral. 82 (1997) 51.
[33] Y.L. Wang, K. Duncan, E.D. Wachsman, F. Ebrahimi, Solid State Ionics 178 (2007) 53.
[34] L. Minervini, M.O. Zacate, R.W. Grimes, Solid State Ionics 116 (1999) 339.
[35] H. Barnighausen, G. Schiller, J. Less-Common Met. 110 (1985) 385.
[36] R. Wyckoff, Crystal Structures, Interscience, New York, 1963.
[37] C.H. Cheng, S.F. Lee, C.W. Hong, J. Electrochem. Soc. 154 (2007) E158.
[38] H. Hayashi, R. Sagawa, H. Inaba, K. Kawamura, Solid State Ionics 131 (2000) 281.